Influence of pre-existing microstructure on mechanical properties of marine ice during compression experiments

Marie DIERCKX,[1] Mark PETERNELL,[2] Christian SCHROEDER,[3] Jean-Louis TISON[1]

[1] *Laboratoire de Glaciologie, Université Libre de Bruxelles, Brussels, Belgium*
E-mail: mdierckx@ulb.ac.be
[2] *Institute of Geosciences, University of Mainz, Mainz, Germany*
[3] *École Polytechnique de Bruxelles, Université Libre de Bruxelles, Brussels, Belgium*

ABSTRACT. Marine ice is an important component of ice shelves in Antarctica. It accretes in substantial amounts at weak points and below ice shelves. It is likely to exhibit peculiar rheological properties, which are crucial to understanding its potential role in stabilizing ice-shelf flow. Due to its location and consolidation processes, marine ice can present a variety of textures which are likely to influence its rheological properties. We present a new dataset of unconfined uniaxial compression experiments on folded marine ice samples that have been cut at various angles to the folds. Texture and fabric analyses are described 'before' and 'after' the deformation experiment. It is shown that, in the given stress configuration, the geometry of the anisotropy controls the rheological behaviour of the marine ice. During secondary creep, folded marine ice is harder to deform than weakly textured ice when compressed parallel or perpendicular to the folds' hinges, while the reverse is true for ice compressed at 45°. The observed range of values for the *n* exponent in Glen's flow law is between 2.1 and 4.1. Surprisingly, we see that tertiary creep tends to develop at a higher total strain than for randomly oriented impurity-free meteoric ice.

KEYWORDS: Antarctic glaciology, applied glaciology, ice rheology, ice shelves, ice/ocean interactions

INTRODUCTION

Ice shelves play a crucial role in the global stability of Antarctica, regulating ice flux from the continent to the ocean (e.g. Scambos and others, 2004; Greve and Blatter, 2009; Rignot and others, 2013). Marine ice is one component of these ice shelves and is known to make up a significant fraction of their mass (e.g. Fricker and others, 2001; Joughin and Vaughan, 2004; Craven and others, 2009; Holland and others, 2009; Jansen and others, 2012). It results from the consolidation of loose frazil ice forming under supercooling in the outflowing ice-shelf water branch of the Deep Thermohaline Circulation (Jacobs and others, 1992). It can accrete rapidly and in large amounts in 'weak' areas of the ice shelf (e.g. bottom crevasses at the grounding line, suture zones between individual ice streams feeding into the ice shelf, frontal rifts, sides of pinning points or longitudinal suture zones; Morgan, 1972; Oerter and others, 1992; Eicken and others, 1994; Fricker and others, 2001; Khazendar and Jenkins, 2003; Craven and others, 2009; Jansen and others, 2012, 2013). Marine ice then slowly consolidates by heat conduction. Because of these particular formation conditions, marine ice has specific intrinsic properties. Several detailed studies have described and compared them to meteoric ice (Moore and others, 1994; Oerter and others, 1994; Souchez and others, 1995; Tison and others, 1998; Khazendar and others, 2001; Treverrow and others, 2010, and references therein). Marine ice is two orders of magnitude more saline than meteoric ice and two orders of magnitude less saline than sea ice. It shows a positive $\delta^{18}O$ signature because it is formed from the freezing of sea water. It is devoid of gas bubbles but can contain solid inclusions of marine or detritic origin, which can potentially form liquid-filled inclusions (Craven and others, 2005, 2009). Marine ice presents a whole range of ice fabrics (known as the crystallographic preferred orientation, CPO), which result from a combination of accretion and deformation processes. This suggests that marine ice could impact the ice-shelf rheology because of its specific properties.

In a recent paper, Dierckx and Tison (2013) have shown that the rheology of weakly textured marine ice can be described as the lower boundary of ice viscosity in the generalized flow law relationship of Cuffey and Paterson (2010). In the same work, it is also shown that for the studied stress-field geometry and intensity, bulk salinity is not a significant controlling factor during marine ice deformation experiments. However, although marine ice thin sections are rarely described in the literature, it is clear from field observations in the Terra Nova Bay area (Tison and others, 1993; Khazendar and others, 2001; Samyn and others, 2007; Dierckx and Tison, 2013) that marine ice often shows a strong anisotropy. Marine ice accretion occurs under ice shelves in very different geometrical settings, such as transverse basal crevasses or rifts at grounding lines, longitudinal 'suture zones' between feeder ice streams, rifts at the ice-shelf front, shear zones around pinning points and at the bottom of the ice shelf. Therefore, it is likely to be submitted to different stress fields, such as longitudinal compression, longitudinal extension, lateral compression and lateral shear, and varying stress intensity. To our knowledge, no case study exists to date that documents the potential dependency of marine ice rheology on its pre-existing microstructure. This paper describes the mechanical properties of naturally pre-oriented marine ice samples in uniaxial unconfined compression, as a function of the initial anisotropy and of the relative orientation of the sample in the applied stress field. Results are compared with those obtained by Dierckx and Tison (2013) for weakly textured

https://doi.org/10.3189/2014JoG13J154 Published online by Cambridge University Press

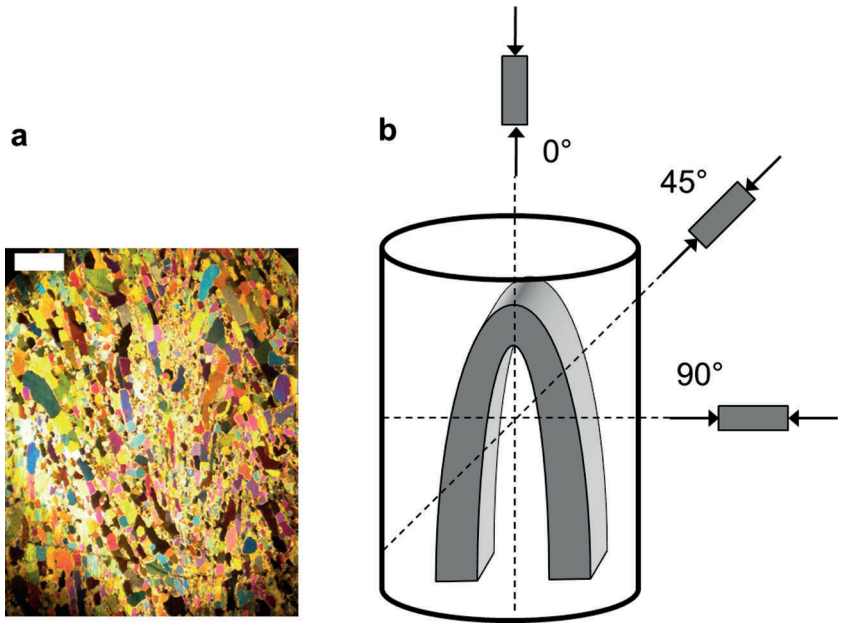

Fig. 1. (a) Typical thin section of folded marine ice (NIS). The white bar scale represents 1 cm. (b) Schematic showing the folding direction of the marine ice samples in the original ice core, as well as the different compression axes used in the experiment.

samples. The deformation experiments are supported by a detailed comparison and analysis of the marine ice microstructure 'before' and 'after' compression experiments. For that purpose, we use a Russell-Head G50 automatic fabric analyzer (Wilson and others, 2003, 2007) in combination with the new 'FAME' (Fabric Analyser based Microstructure Evaluation) toolbox (Peternell and others, 2014) in order to give a full, statistically based description of grain sizes, crystal orientation and geometry for each sample.

SITE DESCRIPTION

The marine ice samples were retrieved from the Nansen Ice Shelf (NIS), located in Terra Nova Bay, East Antarctica (Khazendar, 2000; Khazendar and others, 2001; Tison and others, 2001). There, rifts transverse to the ice-shelf flow open throughout the entire ice thickness (of a few hundred metres) and marine ice typically accumulates. Marine ice consolidates inside the rifts at the grounding line, flows downstream, and outcrops at the ice-shelf surface at all times, due to net ablation from severe katabatic wind regimes. The NIS1 45 m ice core was collected during the 1995/96 austral summer in the framework of a Belgian–Italian drilling programme. It was located along the central flowline of the ice shelf at 7.5 km (74°51′ S, 162°50′ E), downstream of the grounding line (Khazendar and others, 2001). It had a diameter of 8 cm and was collected with an electromechanical (SIPRE-type) ice corer.

METHODOLOGY

Sample selection

Naturally pre-oriented marine ice samples were selected on the basis of their initial microstructure, using standard microtoming procedures (Langway, 1958) to produce thin sections that were further analyzed on a G50 LED-White automated fabric analyzer (Wilson and others, 2007; Wilson and Peternell, 2011). Weakly textured (WT) samples from the NIS1 ice core have already been presented in a previous study, which compared the viscosities of WT marine ice with artificial and meteoric isotropic ice samples within the –10 to –3°C temperature range (Jacka, 1984; Budd and Jacka, 1989; Jacka and Li, 1994; Dierckx and Tison, 2013). Here we specifically selected visually folded (F) samples displaying a sub-vertically folded microstructure (Fig. 1a). In order to simulate various stress geometries as compared to the 'in situ' folds geometry, we shaped the cylindrical samples along three reference long axes, oriented at 0°, 45° and 90° to the vertical core axis (Fig. 1b). Table 1 lists the initial properties and compression settings for the marine ice samples used in this study.

All thin sections were cut through the vertical axis parallel to the applied stress, rather than parallel to the long axis of the core. This eases the comparison of texture and fabric patterns 'before' and 'after' compression.

Sample microstructure and analysis

The initial grain size was similar for all samples, with an overall mean value of the diameter of 0.54 mm (Table 1). All thin sections were analysed using the FAME toolbox (Peternell and others, 2014). This MATLAB® toolbox extracts several properties from the crystal raw optical data of the G50, such as grain *c*-axis orientation, grain shape and grain size. Figure 2 illustrates these parameters for WT ice (Fig. 2, column 1) and F ice for samples cut in the 0° (Fig. 2, column 2), 90° (Fig. 2, column 3) and 45° (Fig. 2, column 4) directions from the original ice-core axis.

The upper and lower panels in Figure 2 show the data 'before' and 'after' the deformation experiments. Figure 2a and f show the vertical thin sections in artificial colours (visualizing the degree of orientation) obtained from the G50. Figure 2b and g plot the optical axes for all crystals with a >50% degree of quality in an equal-area Schmidt diagram projected in the vertical plane. In order to detect potential contrasts in behaviour between larger and smaller grains/crystals, the population is split into two groups using the median value of the grain-size distribution (Fig. 2c and h).

https://doi.org/10.3189/2014JoG13J154 Published online by Cambridge University Press

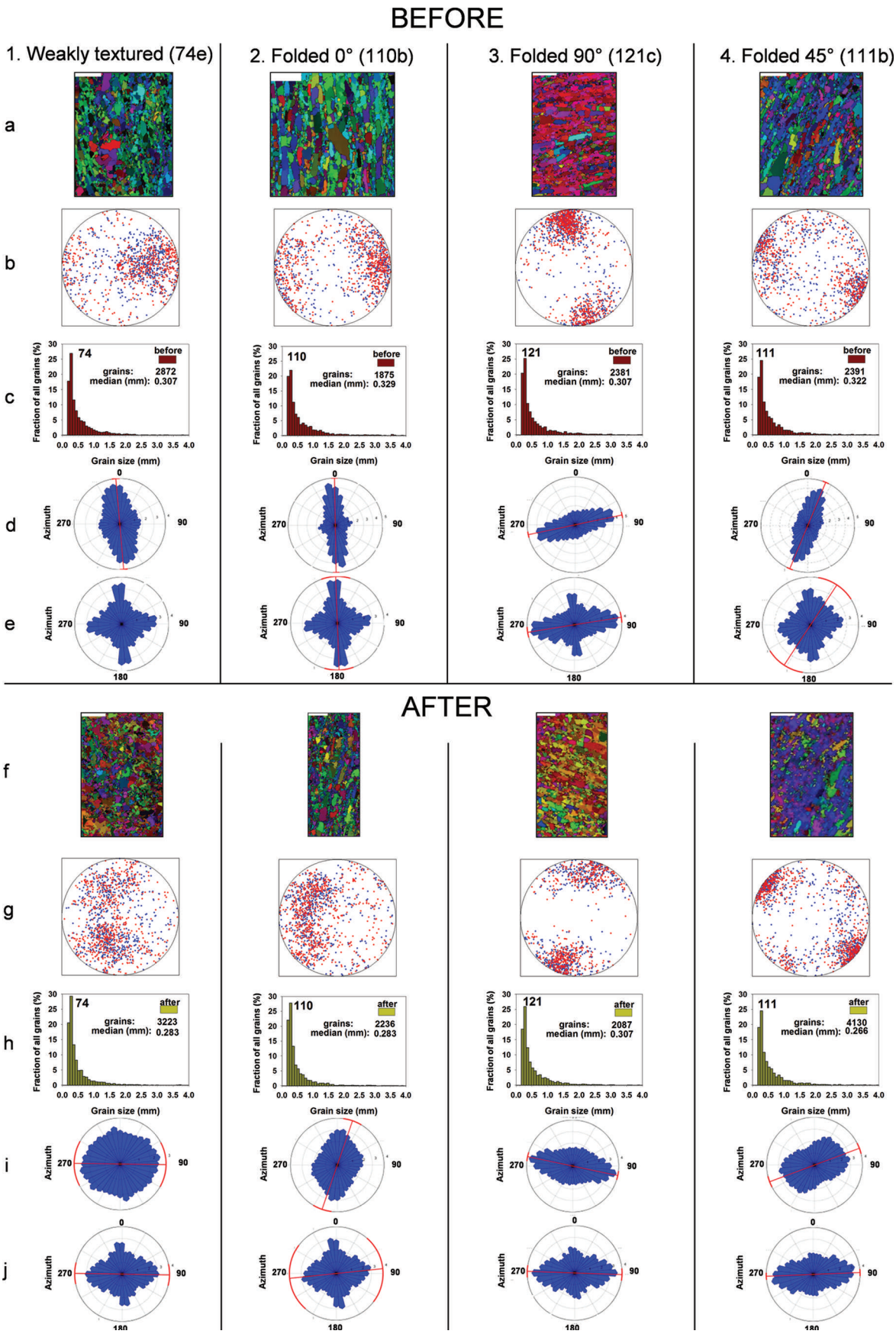

Fig. 2. Marine ice microstructural properties 'before' (a–e) and 'after' (f–j) compression experiments at −6°C for (1) weakly textured samples deformed at 0° (74e), (2) folded (F) samples deformed at 0° (110b), (3) F samples deformed at 90° (121c) and (4) F samples deformed at 45° to the vertical core axis (111b). (a, f) Vertical thin sections shown with artificial colour from the G50-FA software. 1 cm scale is shown as a white strip in upper left corner. The other graphs are calculated by FAME (Peternell and others, 2014). (b, g) Schmidt equal-area projection of *c*-axes from all crystals in the vertical plane; blue and red dots are for the big and small grains respectively. (c, h) Histogram of grain frequency in each grain-size class (bin size of 0.08 mm). (d, i) Rose diagram of grain-shape preferred orientation for the group of larger grains. (e, j) Rose diagram of grain-shape preferred orientation for the group of smaller grains.

https://doi.org/10.3189/2014JoG13J154 Published online by Cambridge University Press

Table 1. Initial properties and compression settings for the weakly textured (WT) and folded (F) marine ice samples used in this study

Sample	Texture and compression axis	Salinity	Mean grain size
			mm
NIS1 97d	WT	0.035	–
NIS1 74e	WT	0.051	0.51
NIS1 59c	WT	0.089	–
NIS1 91b	WT	0.057	–
NIS1 110b	F 0°	0.052	0.57
NIS1 110c	F 0°	0.063	0.55
NIS1 107d	F 90°	0.069	0.50
NIS1 121c	F 90°	0.042	0.54
NIS1 121d	F 90°	0.046	0.54
NIS1 111b	F 45°	0.064	0.53

Red and blue dots are for small and big grains, respectively. From these distribution characteristics, second-rank orientation tensor eigenvalues, $a_{1,2,3}$, can be retrieved. They are summarized in Table 2 for the samples shown in Figure 2. Table 3 (Appendix) provides the eigenvalues for the complete folded sample set. These are given by three orthogonal unit vectors along the axes of an ellipsoid which fits the distribution of *c*-axes (Woodcock, 1977; Durand and others, 2006; Schulson and Duval, 2009). After normalization, the three eigenvalues follow the relationship

$$\begin{aligned} &a_1 + a_2 + a_3 = 1 \\ &\text{with} \\ &0 \leq a_3 \leq a_2 \leq a_1 \leq 1 \end{aligned} \tag{1}$$

If one of these eigenvalues is larger, it means that the ice shows a preferred orientation. Isotropic samples are therefore characterized by an equivalent eigenvalue in each direction, each close to 1/3.

Figure 2c and h show distributions of grain sizes (diameters). For each grain size (here in 0.08 mm increments) the graphs plot the fraction (%) of the total number of grains in a given size range. The number of crystals and median grain sizes are indicated on the graph. The structural orientation of the grain is also represented by the shape preferred orientation (SPO). Crystal SPO is plotted as a 'rose diagram', in Figure 2d/i and e/j for larger/smaller grains. In these diagrams, each individual radial blue bar represents a 10° azimuthal bin. The radial length of each bar gives the percentage of grains with the principal SPO falling into a given azimuthal bin. Since SPO describes an axis, bins [180–360°] are symmetrical with bins [0–180°]. The red line represents the mean azimuth of the principal SPO. Associated confidence intervals of 1σ are shown as red curves on each side of the principal SPO.

Compression experiments

Our study was carried out at a fixed temperature of –6°C. The samples were deformed in unconfined uniaxial compression using the pneumatic device developed at the Laboratoire de Glaciologie, Université Libre de Bruxelles (Samyn and others, 2011). Samples were cylindrical, ~3.5 cm in diameter and ~7 cm high. The aim of the deformation experiments is to reach secondary creep at which the strain rate is minimal. Minimum creep is a unique point within the ice creep curve, that allows comparison between the effects of the properties of various ice types. Each sample is submitted stepwise to increasing stress, beginning with a stress close to 0.1 MPa and incrementing up to a maximum of 0.8 MPa. This procedure allows us to use the same sample for different applied stresses, and therefore to keep the same *A* parameter, which is sample-dependent, in order to only analyse parameter *n* in Glen's flow law (Glen, 1955, 1958):

$$\dot{\epsilon} = A\sigma^n \tag{2}$$

where $\dot{\epsilon}$ is the strain rate and σ the applied stress. A typical strain vs time curve, which includes the different stress steps, is presented in Figure 6 (Appendix). Although we measured stresses up to 0.8 MPa, careful inspection of the data shows that the curve generally departed from perfectly linear behaviour (characteristic of secondary creep) at octahedral shear stresses exceeding 0.4 MPa. For consistency, therefore, steps at higher stresses were not used in the determination of the *n* parameter. One should, however, bear in mind that the real gauge for the transition to tertiary is the total accumulated strain. The stress limit used here is therefore valid only for these experiments. It should be noted that the samples 'after' deformation have started transition to the tertiary creep stage. This will be important in the interpretation of the post-deformation microstructure. At each step where the secondary creep stage is reached, we record the associated minimum strain rate for each stress level. Using secondary rather than tertiary creep means that pre-oriented fabric can play a role in the viscosity, resulting in dispersion in the dataset. Combining these stepwise records in a log–log plot of $\dot{\epsilon}$ vs τ_{oct}, where τ_{oct} is the octahedral shear stress (as in Fig. 4), allows an easy representation of Glen's flow law, to deduce values for the *n* and *A* parameters. Octahedral strain rate and shear stress (Cuffey and Paterson, 2010) are used here and ease comparison with previous studies. Dierckx and Tison (2013) confirmed the validity of this stepwise load approach. It is interesting to note that the transition to tertiary creep typically occurred at total accumulated strain values of 3–4%, which are relatively high compared with randomly oriented impurity-free meteoric ice, where the secondary creep minimum is often found at ~1% of octahedral shear strain (Budd and Jacka, 1989). The observation of Treverrow and others (2010) supports the concept of a reduced rate of microstructural evolution. This could be a factor in observing a secondary creep minimum occurring at higher strain.

Table 2. Second-rank orientation tensor eigenvalues of Figure 2b and g. The complete list for all folded samples is given in Table 3 (Appendix)

Sample ID	'Before'			'After'		
	a_1	a_2	a_3	a_1	a_2	a_3
NIS1 74e	0.55	0.25	0.19	0.51	0.34	0.14
NIS1 110b	0.46	0.32	0.22	0.50	0.35	0.15
NIS1 121c	0.67	0.21	0.11	0.62	0.26	0.11
NIS1 111b	0.51	0.28	0.21	0.56	0.24	0.19

Salinity

The salinity of each sample was determined by Cl^- anion measurements (HPLC; high-performance liquid chromatography, Dionex 100, precision ≤4%). Bulk ice salinity is deduced from the mean C^-/salinity ratio in sea water

https://doi.org/10.3189/2014JoG13J154 Published online by Cambridge University Press

(19.35/35), assuming that the Cl^-/salinity ratio does not change during the formation or melting of marine ice samples (Sarmiento and Gruber, 2006). This approximation is of limited accuracy, but we consider it sufficient for the purposes of this paper.

Density

Densities have been estimated with a precise volumetric method (error ±2%) on nearby samples (~10 cm above or below the deformed samples) and are listed in Table 4 (Appendix). Values range between 897 and 927 kg m^{-3} (±2%). These nicely frame the theoretical value of 919 kg m^{-3} for pure ice at –20°C, and are clearly higher than the value of 836 kg m^{-3} expected for meteoric ice with an air content of 90 mL kg^{-1}.

RESULTS AND DISCUSSIONS

Microstructure

In this section, we discuss the potential textural and structural changes 'before' and 'after' our compression experiments. It is important to note that the data are unavoidably based on different thin sections, always spaced a few centimetres apart. Given the heterogeneity of marine ice at NIS, some of the observed differences might therefore simply result from spatial variability. We will therefore focus on the main contrasts and coherent features between samples.

Pre-deformation

Although visually different, all samples show strong similarities: *c*-axes display a relatively strong single maximum, roughly oriented perpendicular to the ice-core vertical axis. Eigenvalues (Tables 2 and 3) confirm the general structure of a wide single maximum for all samples, with $a_1 > a_2 > a_3$ and moderate a_1 values. Small differences in *a* values reveal different levels of spreading of the single maximum. Grains are predominantly very small (mean diameter ~0.50 mm), with a tail towards larger crystals. These probably bias the visual inspection. Large grains show a strong elongation, with SPO parallel to their basal planes and approximately perpendicular to the *c*-axis single maximum. This elongation reflects the accretion of neighbouring grains of similar *c*-axis orientation into larger single grains, in combination with preferential growth of single crystals along their basal plane by grain migration processes. The small-grain distribution is clearly bimodal, with one preferred azimuth coherent with that of the larger grains and the other, less strong, perpendicular to it.

To understand these initial properties one needs to recall the process of marine ice formation at NIS (Khazendar and others, 2001). As the rift opens at the grounding line (near Teall Nunatak; fig. 1 of Khazendar and others, 2001), ice-shelf water presumably invades it, generating large amounts of tiny frazil ice crystals at high rates (Khazendar and Jenkins, 2003). Localized supercooling within the rift also contributes to the formation of the frazil crystals. As this mixture of individual ice crystals and water consolidates, the ice moves downstream and the rift closes under local longitudinal compression. This wet metamorphism of a porous ice crystals/sea-water mix at high temperature (initially sea-water freezing point) has, to our knowledge, never been properly described in the literature. It should differ significantly from the better-documented processes of cold dry snow metamorphism in ice sheets, although even these are still under discussion, as far as activation thresholds of microstructural processes, such as grain rotation, polygonization and grain boundary migration, are concerned (e.g. Durand and others, 2007, 2009). Therefore the interpretation here remains conjectural for our textural observations. Ice growth in a water-filled porous medium might have favoured elongation of some of the crystals along their basal planes. These grains would have more readily rotated within the mix, perpendicular to the longitudinal compression under cumulative strain, generating the broad single maximum and the sub-vertical SPO for the large grains.

As suggested by the comparison of small vs large grains' *c*-axis plots (red vs blue dots in Fig. 2b), rotation and elongation also involve the smaller grains. However, as shown by the 'cross shape' of the small-grain azimuthal distribution (Fig. 2e), part of that (sub-millimetre) population shows a SPO closer to the horizontal plane. This could be interpreted as the inherited signature of the deposition process of the individual ice crystals, with a 'normal' distribution around the horizontal, as might be expected from individual disc-like crystals, buoyancy and rearrangement under increasing upward buoyancy stress. This 'primary' depositional layering would have been preserved in the pockets of material between zones of larger crystals. The noticeable changes observed after our compression experiments (with SPO not found in the original material) suggest moderate internal deformation within the ice shelf once the whole marine ice inclusion has been consolidated.

Sample 74e was interpreted as 'weakly textured', based on the visual grain texture (Fig. 2a, column 1). However, detailed crystallographic analysis demonstrates that, although different, weakly textured and folded samples share some similarities. The SPO of the large grains is less pronounced in WT (Fig. 2d), and visual interpretation of the *c*-axis diagrams suggests the occurrence of more randomly oriented crystals, compared to the fabric of the other samples. The Schmidt diagram (Fig. 2b) shows a broad distribution of *c*-axes which, nevertheless, gather around a maximum. This confirms the note of Dierckx and Tison (2013) on the challenge of finding purely isotropic fabrics in marine ice at NIS.

It also highlights the potential of high-resolution automated fabric analysis, allowing interpretation that is less biased towards macroscopic features. It should, however, be stressed that the grain-size detection procedure of the FAME software (Peternell and others, 2014) could underestimate grain size in the range close to the fabric analyzer resolution (for this study 1 pixel = 43 μm × 43 μm). This particularly concerns areas such as grain boundaries, where many extremely small grains may be present.

Post-deformation

Despite the fact that the samples started the transition to tertiary creep, we see in Table 2 that the eigenvalues for each sample did not change significantly. Table 3 (Appendix) lists the change of eigenvalues for all folded samples and confirms this observation. Although we cannot be sure to what extent each sample ventured into tertiary creep, we assume here that microstructural changes towards tertiary creep have been initiated. However, it remains important to understand how compression along the different axes of the folds influences the development of a new microstructure. In terms of *c*-axis fabrics (Fig. 2g), the WT sample 74e appears

https://doi.org/10.3189/2014JoG13J154 Published online by Cambridge University Press

to have evolved towards 'dispersion' and perhaps a dual maximum. The folded sample 110b deformed along the vertical axis direction (0°) shows a similar pattern. Sample 121c, compressed perpendicular to the dominant crystal elongation, i.e. coherent with the initial 'in situ' configuration, shows the least changes, apart from a different tilt; that, however, might result from spatial variability. Sample 111b, compressed at 45° (i.e. with pre-elongated crystals along the direction of the newly applied maximum shear), keeps the initial fabric, but adds a secondary maximum oriented at 90° to the initial maximum. This is to be expected if new grains develop along both maximum shear directions. The maximum perpendicular to the pre-oriented crystals elongation is nevertheless likely to remain dominant and be reinforced (see a_1 value in Table 2). However, these changes have minimal impact on the calculated eigenvalues.

The most obvious changes occur in the grain-size distribution and grain SPO. Figure 3 compares frequency distributions 'before' and 'after' compression, both for the number of grains (Fig. 3a, which shows the same data as Fig. 2c and h) and thin-section area coverage of a given grain-size class (Fig. 3b). For all experiments, but at different degrees of intensity, the number of crystals with lower grain sizes increases, as well as their area coverage. This is to be expected, since our samples have started the transition to tertiary creep. At the same time, the SPO of all samples is rotated towards the 90–270° direction (Fig. 2d and e vs Fig. 2i and j), which is perpendicular to the new applied stress. This is in accordance with Wilson and Peternell (2011), who showed that the initial SPO in layered ice is already significantly changed during the first 1–2% accumulated strain. The main driving factor for this behaviour is nucleation of new grains together with their grain boundary migration driven growth (Wilson and Peternell, 2011). This results in a weaker SPO for the samples with their initial SPO parallel to the experimental compression (74e, 110b), and with limited changes for the sample oriented at 90° (121c).

To summarize, our experiments mainly accommodated the new stress field by reducing mean grain size, with minimal changes in the original fabric, since it is only the beginning of the transition to tertiary creep. At this stage, it remains difficult to assess whether subgrain boundary rotation recrystallization or grain boundary migration recrystallization is the cause of this grain-size decrease (Durand and others, 2009, and references therein). Grain boundary migration recrystallization probably started in the 45° experiment, where new crystals appeared at high angles to the pre-existing fabric, but at the expected position, considering the newly applied stress field (Peternell and others, 2014).

Rheological behaviour

Figure 4 summarizes the results of our set of compression experiments in a $\log \dot{\epsilon}_{oct}$ vs $\log \tau_{oct}$ diagram. Figure 4a reproduces the –6°C dataset of Dierckx and Tison (2013), and Figure 4b, c and d show the deformation experiments with compression axes at 0°, 45° and 90°, respectively, of the ice-core vertical axis. The slope and intercept of the linear regressions correspond to n and $\log A$ in Glen's flow law, respectively. As explained above, only the data points below 0.4 MPa were used to determine n.

As demonstrated by Dierckx and Tison (2013), WT marine ice rheology is well approximated by Cuffey and Paterson's (2010) temperature/viscosity relationship, shown as a black line with slope $n = 3$ in Figure 4a. This trend will be used as a reference for the folded samples in this study (grey lines in Fig. 4b–d).

Submitting folded samples to uniaxial compression results in different behaviour depending on the stress geometry. Figure 4b shows the case for a sample cut parallel to the ice-core axis. In that configuration, the ice is compressed parallel to the principal grain elongation, i.e. parallel to the basal plane of the crystals, while the maximum shear-stress planes are located at 45°. The ice appears harder than its WT equivalent at all applied stresses and throughout secondary creep, in the stress condition studied. The data points up to 0.4 MPa fit Glen's law with $n = 3.2 \pm 0.2$. Once secondary creep is exceeded (which occurs slightly above 0.4 MPa in our experiments), we consider no further data points. At this stage, cumulative strain and increased stress will bring the sub-vertical elongated grains closer to the maximum shear planes (compare Fig. 2d and i with Fig. 2e and j). This will lead to a reduction in grain size and recrystallization by subgrain boundary rotation recrystallization and eventually grain boundary migration and/or nucleation.

Compressing the sample at 90° to the principal grain elongation (Fig. 4d) results in an exponent $n = 4.1 \pm 0.2$. However, because most of the crystals are initially elongated along the final orientation at higher strains, the ice actually gets softer than WT ice above 0.3 MPa octahedral shear stress (at large total accumulated strain), while it is harder at lower stresses (lower total strain). This stress configuration appears to be coherent with the stress history of the marine ice while it was consolidating in the closing rift. It is interesting to note that, in the 90° cases, the final sample shape was turned into a parallelogram, with sides twisted up to 10° on the vertical compressive axis. The geometry of the sample and of its crystalline structure has favoured a shearing experiment rather than a compressive experiment. This is probably a consequence of the onset of the transition/tertiary stage.

Finally, Figure 4c shows the intermediate case, where the ice is compressed at 45° to the vertical core axis. This implies that the principal grain elongation (i.e. the crystal basal plane) is now roughly parallel to the maximum applied shear stress. Even with the limited number of data points, it is clear that the ice is softer than the WT ice throughout secondary creep. A fit of these few points leads to an exponent $n = 2.1 \pm 0.2$.

The values of $n = 4.1 \pm 0.2$ and 2.1 ± 0.2 for the 90° and 45° experiments, respectively, are in remarkably good agreement with the findings of Manley and Schulson (1997), who found n values of 4.6 and 2.2 for ice samples with elongated grains compressed perpendicular to the grain long axis and at 45° to it, respectively. As can be seen, this is close to the configuration of the elongated marine ice grains from our study, which we compressed at 90° and 45°.

Large-scale implications

Figure 5 summarizes potential locations for field equivalents of the applied experimental stress configurations. As mentioned above, marine ice accretes as loose frazil ice crystals in various locations and further consolidates and deforms within the local stress field. Just downstream of the grounding line (where drastic changes in basal friction generate transverse vertical bottom crevasses or even rifts) marine ice is submitted to longitudinal compression as

https://doi.org/10.3189/2014JoG13J154 Published online by Cambridge University Press

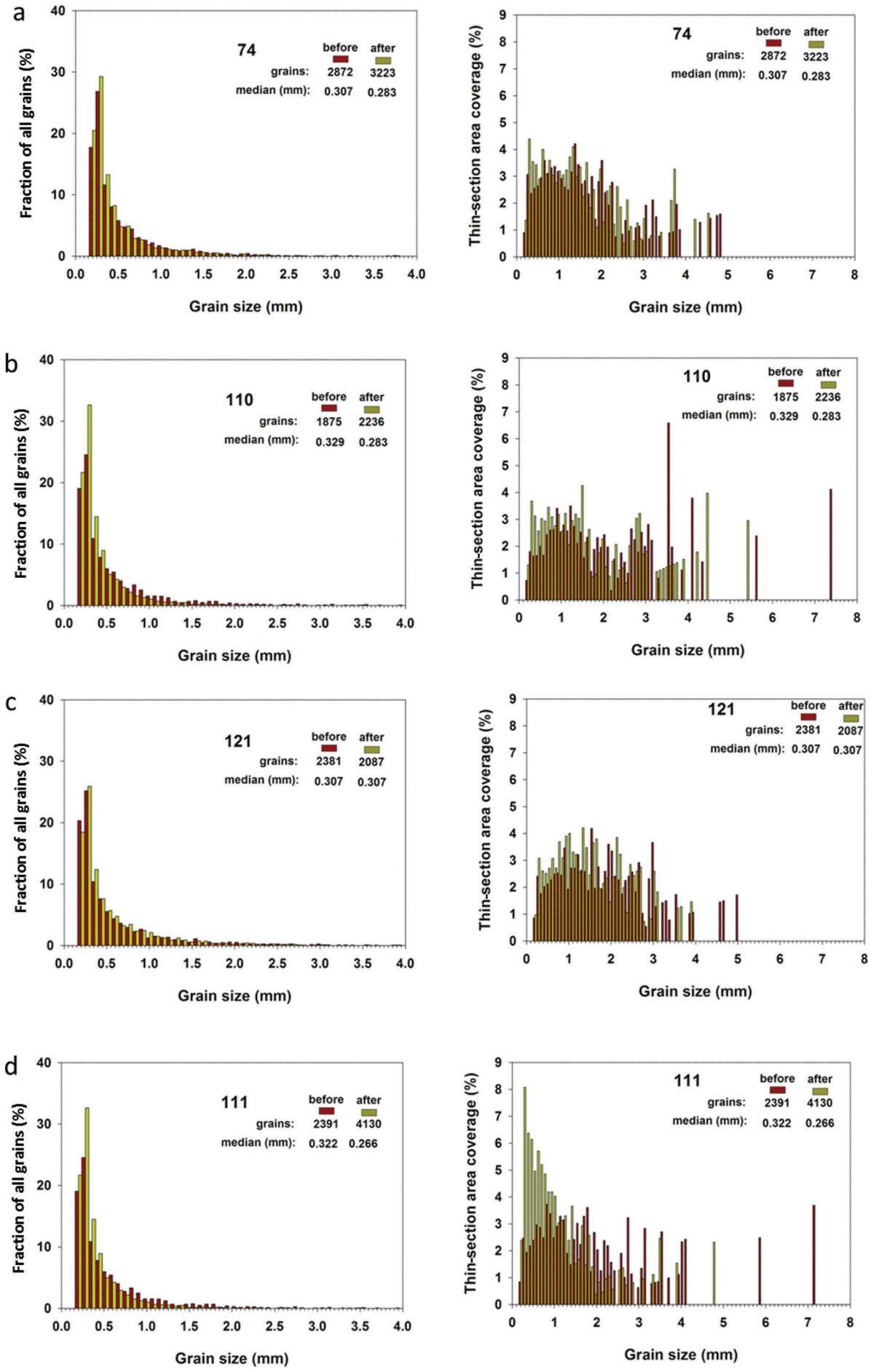

Fig. 3. Grain-size distribution and area coverage 'before' and 'after' the compression for the different cases: weakly textured (74), folded 0° (110), folded 90° (121) and folded 45° (111).

https://doi.org/10.3189/2014JoG13J154 Published online by Cambridge University Press

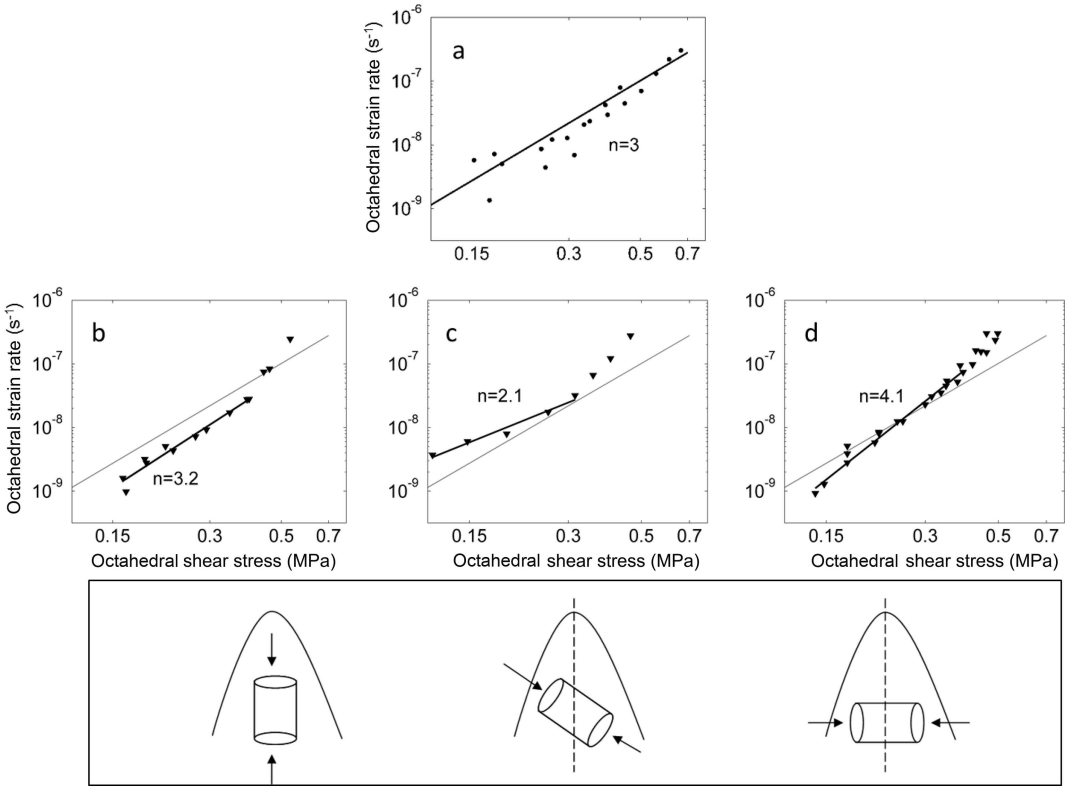

Fig. 4. Octahedral shear strain rate as a function of octahedral shear stress for the marine ice compression experiments. (a) Summary of the Dierckx and Tison (2013) experiments (dots) with Cuffey and Paterson's (2010) relationship shown as the straight line. (b–d) Results from compression experiments on folded samples (this study) with compression axes at 0°, 45° and 90° to the ice-core vertical axis, respectively, as sketched in the bottom panel. Triangles: data points; grey line: Cuffey and Paterson's (2010) relationship as in (a); solid black line: linear regression for all steps occurring during secondary creep. The confidence interval for *n* for all regressions is ±0.2.

the rifts/crevasses close, a process illustrated by the observed sub-vertical folds (Figs 1a and 5, A). As shown by Dierckx and Tison (2013), as long as the texture and fabrics remain weakly textured the ice represents the 'hardest' case in Cuffey and Paterson's (2010) relationship. However, as folds and sub-vertically elongated crystals develop (Fig. 2, column 3; our 90° experimental set-up), the ice gets harder (Fig. 4d) at low stresses. Further downstream, and away from convergence areas of former ice streams or glaciers (Fig. 5, B), the stress field returns to a 'classical' ice-shelf configuration with longitudinal extension and vertical compression parallel to the fold planes. In this case (0° experimental set-up, Fig. 2, column 2) ice becomes even harder and remains so throughout secondary creep and until 0.4 MPa (Fig. 4b). In contrast, in the vicinity of former ice-stream/glacier suturing, either at the tip of curved old transverse crevasse fillings (Fig. 5, C; see also fig. 1 of Khazendar and others, 2001) or in marine ice bodies squeezed between two ice streams (Fig. 5, D), simple shear associated with differences in longitudinal ice velocities might develop configurations similar to our 45° experimental set-up (Fig. 2, column 4). There, the ice becomes softer than in a weakly textured case, a result in accordance with conclusions drawn from inverse modelling (Khazendar and others, 2009).

CONCLUSION

The frequency of appearance within ice shelves and the specific rheology of marine ice remains largely unknown. Observations, inverse modelling and environmental conditions for its accretion suggest it might represent a significant share of many ice shelves around Antarctica and potentially affect their rheological behaviour. Although it has been shown to represent the hardest version of natural ice (Dierckx and Tison, 2013), its generic setting (bottom crevasses, suture zones between individual ice streams, sides of ice rises, large-scale accretions under positive buoyancy at the bottom of ice shelves) and wet metamorphism favour textural and structural anisotropy with grain elongation and, potentially, the development of folds. We have shown here that, away from suture zones, sides of

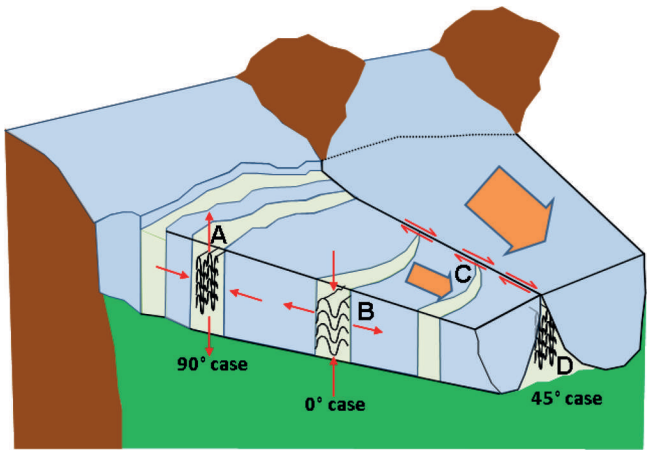

Fig. 5. Sketch of potential locations for field equivalents of applied experimental stress configurations.

https://doi.org/10.3189/2014JoG13J154 Published online by Cambridge University Press

embayments or along ice rises, anisotropy will generally increase marine ice viscosity during secondary creep. The reverse, however, is true along major shear zones (i.e. suture zones, sides of embayments or along ice rises). Anisotropy also alters the *n* exponent of Glen's flow law, which shows values fluctuating between 2.1 and 4.1.

In all cases, it is important to bear in mind that the rheological contrasts discussed here, which are largely driven by the total accumulated strain and microstructure evolution, are strongly dependent on the material properties. These effects clearly need to be combined with the strong temperature dependency of the *A* factor in Glen's flow law. Our dataset provides new settings for modelling exercises that should attempt to test the rheological significance of these specific properties of marine ice bodies. This should be associated with the thermomechanical context of nonlinear vertical ice temperature profiles due to bottom accretion of large amounts of ice, initially at sea-water pressure-melting point. Temperature-dependent compression experiments should be devised to support the modelling effort.

ACKNOWLEDGEMENTS

M.D. is funded by the IceCubeDyn project (Academic Research Collaboration) of the Communauté française de Belgique (Belgium). The compression device was supported by the Antarctic Subglacial Processes and Interactions programme (2006–08) of Belgian Science Policies (SD/CA/02B). We thank the Prix Fonds David et Alice Van Buuren for supporting M.D. in this work. The Italian Antarctic programme (PNRA) and A. Bondesan are warmly thanked for logistic and scientific support during sampling of the NIS1 ice core. We also thank F.-X. Masson for his help. Finally, we thank A. Treverrow and an anonymous reviewer for helpful comments which greatly improved the manuscript.

REFERENCES

Budd WF and Jacka TH (1989) A review of ice rheology for ice sheet modelling. *Cold Reg. Sci. Technol.*, **16**(2), 107–144 (doi: 10.1016/0165-232X(89)90014-1)

Craven M and 7 others (2005) Borehole imagery of meteoric and marine ice layers in the Amery Ice Shelf, East Antarctica. *J. Glaciol.*, **51**(172), 75–84 (doi: 10.3189/172756505781829511)

Craven M, Allison I, Fricker HA and Warner R (2009) Properties of a marine ice layer under the Amery Ice Shelf, East Antarctica. *J. Glaciol.*, **55**(192), 717–728 (doi: 10.3189/002214309789470941)

Cuffey KM and Paterson WSB (2010) *The physics of glaciers*, 4th edn. Butterworth-Heinemann, Oxford

Dierckx M and Tison J-L (2013) Marine ice deformation experiments: an empirical validation of creep parameters. *Geophys. Res. Lett.*, **40**(1), 134–138 (doi: 10.1029/2012GL054197)

Durand G, Gagliardini O, Thorsteinsson T, Svensson A, Kipfstuhl J and Dahl-Jensen D (2006) Ice microstructure and fabric: an up-to-date approach for measuring textures. *J. Glaciol.*, **52**(179), 619–630 (doi: 10.3189/172756506781828377)

Durand G and 8 others (2007) Change in ice rheology during climate variations – implications for ice flow modelling and dating of the EPICA Dome C core. *Climate Past*, **3**(1), 155–167 (doi: 10.5194/cp-3-155-2007)

Durand G and 7 others (2009) Evolution of the texture along the EPICA Dome C ice core. In Hondoh T ed. *Physics of ice core records II*. (Supplement issue of Low Temperature Science 68) Institute of Low Temperature Science, Hokkaido University, Hokkaido, 91–106

Eicken H, Oerter H, Miller H, Graf W and Kipfstuhl J (1994) Textural characteristics and impurity content of meteoric and marine ice in the Ronne Ice Shelf, Antarctica. *J. Glaciol.*, **40**(135), 386–398

Fricker HA, Popov S, Allison I and Young N (2001) Distribution of marine ice beneath the Amery Ice Shelf. *Geophys. Res. Lett.*, **28**(11), 2241–2244 (doi: 10.1029/2000GL012461)

Glen JW (1955) The creep of polycrystalline ice. *Proc. R. Soc. London, Ser. A*, **228**(1175), 519–538 (doi: 10.1098/rspa.1955.0066)

Glen JW (1958) The flow law of ice: a discussion of the assumptions made in glacier theory, their experimental foundation and consequences. *IASH Publ.* 47 (Symposium at Chamonix 1958 – *Physics of the Movement of the Ice*), 171–183

Greve R and Blatter H (2009) *Dynamics of ice sheets and glaciers*. Springer, Dordrecht

Holland PR, Corr HFJ, Vaughan DG, Jenkins A and Skvarca P (2009) Marine ice in Larsen Ice Shelf. *Geophys. Res. Lett.*, **36**(11), L11604 (doi: 10.1029/2009GL038162)

Jacka TH (1984) The time and strain required for development of minimum strain rates in ice. *Cold Reg. Sci. Technol.*, **8**(3), 261–268 (doi: 10.1016/0165-232X(84)90057-0)

Jacka TH and Li J (1994) The steady-state crystal size of deforming ice. *Ann. Glaciol.*, **20**, 13–18

Jacobs SS, Hellmer HH, Doake CSM, Jenkins A and Frolich RM (1992) Melting of ice shelves and the mass balance of Antarctica. *J. Glaciol.*, **38**(130), 375–387

Jansen D, Luckman A, Kulessa B, King EC and Holland P (2012) Flow regime of the Joerg Peninsula suture zone, Larsen C Ice Shelf: the role of marine ice. *Geophys. Res. Abstr.*, **14**, EGU2012-11685

Jansen D, Luckman A, Kulessa B, Holland PR and King EC (2013) Marine ice formation in a suture zone on the Larsen C Ice Shelf and its influence on ice shelf dynamics. *J. Geophys. Res.*, **118**(3), 1628–1640 (doi: 10.1002/jgrf.20120)

Joughin I and Vaughan DG (2004) Marine ice beneath the Filchner–Ronne Ice Shelf, Antarctica: a comparison of estimated thickness distributions. *Ann. Glaciol.*, **39**, 511–517 (doi: 10.3189/172756404781814717)

Khazendar A (2000) Marine ice formation in rifts of Antarctic ice shelves: a combined laboratory study and modelling approach. (PhD thesis, Université Libre de Bruxelles)

Khazendar A and Jenkins A (2003) A model of marine ice formation within Antarctic ice shelf rifts. *J. Geophys. Res.*, **108**(C7), 3235 (doi: 10.1029/2002JC001673)

Khazendar A, Tison J-L, Stenni B, Dini M and Bondesan A (2001) Significant marine-ice accumulation in the ablation zone beneath an Antarctic ice shelf. *J. Glaciol.*, **47**(158), 359–368 (doi: 10.3189/172756501781832160)

Khazendar A, Rignot E and Larour E (2009) Roles of marine ice, rheology, and fracture in the flow and stability of the Brunt/Stancomb-Wills Ice Shelf. *J. Geophys. Res.*, **114**(F4), F04007 (doi: 10.1029/2008JF001124)

Langway CC Jr (1958) Ice fabrics and the universal stage. *SIPRE Tech. Rep.* 62

Manley ME and Schulson EM (1997) On the strain-rate sensitivity of columnar ice. *J. Glaciol.*, **43**(145), 408–410

Moore JC, Reid AP and Kipfstuhl J (1994) Microstructure and electrical properties of marine ice and its relationship to meteoric ice and sea ice. *J. Geophys. Res.*, **99**(C3), 5171–5180 (doi: 10.1029/93JC02832)

Morgan VI (1972) Oxygen isotope evidence for bottom freezing on the Amery Ice Shelf. *Nature*, **238**(5364), 393–394 (doi: 10.1038/238393a0)

Oerter H and 6 others (1992) Evidence for basal marine ice in the Filchner–Ronne Ice Shelf. *Nature*, **358**(6385), 399–401 (doi: 10.1038/358399a0)

Oerter H, Eicken H, Kipfstuhl J, Miller H and Graf W (1994) Comparison between ice core B13 and B15. In Oerter H ed. *Filchner–Ronne Ice Shelf Programme (FRISP). Report No. 7*

(1994) . Alfred Wegener Institute for Polar and Marine Research, Bremerhaven, 29–36
Peternell M, Dierckx M, Wilson CJL and Piazolo S (2014) Quantification of the microstructural evolution of polycrystalline fabrics using FAME: application to in situ deformation of ice. *J. Struct. Geol.*, **61**, 109–122 (doi: 10.1016/j.jsg.2013.05.005)
Rignot E, Jacobs S, Mouginot J and Scheuchl B (2013) Ice-shelf melting around Antarctica. *Science*, **341**(6143), 266–270 (doi: 10.1126/science.1235798)
Samyn D, Remy J-P, Duval P, Montagnat M and Tison J-L (2007) Compression experiments on marine ice from Nansen Ice Shelf, Antarctica: implications for ice-shelf/continent interactions. *Geophys. Res. Abstr.*, **9**, EGU2007-A-00803
Samyn D, Dierckx M, Remy JP, Goossens T and Tison J-L (2011) A simple and updated pneumatic method for uniaxial ice compression in the laboratory: experimental settings and creep test results on glacier ice. *J. Glaciol.*, **57**(202), 337–344 (doi: 10.3189/002214311796405960)
Sarmiento JL and Gruber N (2006) *Ocean biogeochemical dynamics*. Princeton University Press, Princeton, NJ
Scambos TA, Bohlander JA, Shuman CA and Skvarca P (2004) Glacier acceleration and thinning after ice shelf collapse in the Larsen B embayment, Antarctica. *Geophys. Res. Lett.*, **31**(18), L18402 (doi: 10.1029/2004GL020670)
Schulson EM and Duval P (2009) *Creep and fracture of ice*. Cambridge University Press, Cambridge
Souchez R and 6 others (1995) Investigating processes of marine ice formation in a floating ice tongue by a high-resolution isotopic study. *J. Geophys. Res.*, **100**(C4), 7019–7025 (doi: 10.1029/95JC00142)
Tison J-L, Ronveaux D and Lorrain RD (1993) Low salinity frazil ice generation at the base of a small Antarctic ice shelf. *Antarct. Sci.*, **5**(3), 309–322 (doi: 10.1017/S0954102093000409)
Tison J-L, Lorrain RD, Bouzette A, Dini M, Bondesan A and Stiévenard M (1998) Linking landfast sea ice variability to marine ice accretion at Hells Gate Ice Shelf, Ross Sea. In Jeffries MO ed. *Antarctic sea ice: physical processes, interactions and variability*. (Antarctic Research Series 74) American Geophysical Union, Washington, DC, 375–407
Tison J-L, Khazendar A and Roulin E (2001) A two-phase approach to the simulation of the combined isotope/salinity signal of marine ice. *J. Geophys. Res.*, **106**(C12), 31 387–31 401 (doi: 10.1029/2000JC000207)
Treverrow A, Warner RC, Budd WF and Craven M (2010) Meteoric and marine ice crystal orientation fabrics from the Amery Ice Shelf, East Antarctica. *J. Glaciol.*, **56**(199), 877–890 (doi: 10.3189/002214310794457353)
Wilson CJL and Peternell M (2011) Evaluating ice fabrics using fabric analyser techniques in Sørsdal Glacier, East Antarctica. *J. Glaciol.*, **57**(205), 881–894 (doi: 10.3189/002214311798043744)
Wilson CJL, Russell-Head DS and Sim HM (2003) The application of an automated fabric analyzer system to the textural evolution of folded ice layers in shear zones. *Ann. Glaciol.*, **37**, 7–17 (doi: 10.3189/172756403781815401)
Wilson CJL, Russell-Head DS, Kunzi K and Viola G (2007) The analysis of quartz *c*-axis fabrics using a modified optical microscope. *J. Microsc.*, **227**(1), 30–41 (doi: 10.1111/j.1365-2818.2007.01784.x)
Woodcock NH (1977) Specification of fabric shapes using an eigenvalue method. *Geol. Soc. Am. Bull.*, **88**(9), 1231–1236 (doi: 10.1130/0016-7606(1977)88<1231:SOFSUA>2.0.CO;2)

APPENDIX

Table 3 presents the second-rank orientation tensors (eigenvalues) for all visually folded samples and for one of the weakly textured samples (previous study of Dierckx and Tison, 2013; ice sample no longer available for measurements).

For all compression experiments, the sample is submitted stepwise to an increasing stress, as shown on the strain curve (Fig. 6). The red lines represent the linear regression, which determines whether the step is considered to be in the secondary creep regime. For all samples, the first step is considered not to be at secondary creep, since we are not sure to have reached it at that stage. (Thus, the first step occurring at ~1% of deformation is not shown in red in the figure.) The steps at octahedral shear stresses exceeding 0.4 MPa are considered no longer to be in secondary creep, the strain response showing a nonlinear trend, symptomatic of the transition regime towards tertiary creep. This 'stress' threshold is, however, only a proxy for the transition to tertiary creep, which is mainly dependent on the total accumulated strain. In principle, secondary creep could be precisely observed by looking at the strain-rate vs strain curve. However, the strain rates are so low in some experiments (especially at low stresses), that time derivatives of the strain usually lead to large scatter in the strain-rate plot. Hence, we prefer to rely on the slope of the linear part of each stress step to determine the strain rate. However, we always compared the minimum strain rate obtained from the

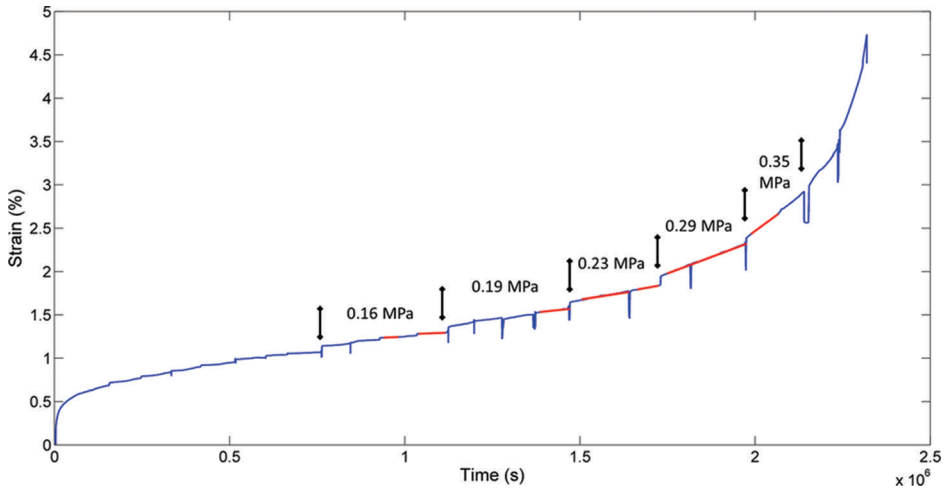

Fig. 6. Strain curve as a function of time for sample NIS1 110b. Red lines represent the linear regressions, which determine whether the step is considered as secondary creep. For each secondary creep step, the related octahedral shear stress is given.

https://doi.org/10.3189/2014JoG13J154 Published online by Cambridge University Press

Table 3. Second-rank orientation tensors (eigenvalues) for all folded samples

Sample ID	'Before'			'After'		
	a_1	a_2	a_3	a_1	a_2	a_3
NIS1 74e	0.555	0.255	0.19	0.51	0.345	0.145
NIS1 110b	0.46	0.32	0.22	0.5	0.35	0.15
NIS1 110c	0.465	0.302	0.233	0.455	0.358	0.187
NIS1 121c	0.675	0.21	0.115	0.625	0.26	0.115
NIS1 121d	0.629	0.239	0.132	0.688	0.224	0.088
NIS1 107d	0.621	0.202	0.177	0.652	0.245	0.103
NIS1 111b	0.51	0.28	0.21	0.565	0.245	0.19

Table 4. Density estimated for the deformed samples at NIS

ID	a_{mean} mm	b_{mean} mm	c_{mean} mm	w_{mean} g	Density kg m^{-3}
NIS1 59d	44.34	46.23	61.33	114.15	908.1
NIS1 74c	45.5	47.15	45.11	89.75	927.23
NIS1 91a	54.01	39.23	58.33	111.32	900.68
NIS1 97c	38.2	52.68	60.72	109.64	897.39
NIS1 107c	41.12	42.05	56.24	87.94	904.44
NIS1 110d	30.83	56.66	51.58	81.28	902.06
NIS1 111a	50.57	38.53	52.05	92.15	908.8
NIS1 121e	44.58	35.94	52.04	75.45	904.87

linear fits of the strain vs time curve with the corresponding regions in the strain-rate vs strain curve.

The marine ice density values have been determined with a precise volumetric method (error ±2%) on nearby samples (~10 cm above or below the deformed samples) and are listed in Table 4, where variables *a*, *b* and *c* are the cube edges and *w* is the weight of this cube. All numbers are a mean value of three repeated measurements.

MS received 28 July 2013 and accepted in revised form 20 March 2014

https://doi.org/10.3189/2014JoG13J154 Published online by Cambridge University Press